

Scattering of Dirac Fermions in Barrier Geometries on the Surface of Topological Insulators

Lindsay Gorman
Princeton University
PACM Independent Work
Adviser: B. Andrei Bernevig
Second Reader: Jason Fleischer

1 Introduction

Predicted theoretically and discovered experimentally, the topological insulators are a new class of materials of particular interest for studying a wide range of issues from fundamental physics of topological order to applications in spintronics and topological quantum computation. These materials are bulk insulators, but maintain robust conducting surface states. The existence of these conducting states on the surface of the material is a direct result of the nontrivial topology of the bulk Hilbert space, under the assumption of time-reversal invariance symmetry. Insulators with time-reversal symmetry can be shown to generically belong to two distinct classes, trivial and non-trivial. Nontrivial topological insulators and the trivial insulating vacuum have wavefunctions which are not smoothly deformable into one another without closing a bulk gap. This difference manifests itself at the interface between the topological insulator and the vacuum. As a result, the surface states are not spurious and cannot be “deformed away”. This renders them robust to any impurity that does not violate the time-reversal symmetry of the bulk material. Potential impurities do not cause backscattering of the edge or surface modes of these new insulators. However, magnetic impurities break time-reversal symmetry and lead to back-scattering.[1][2][3]

As these conducting states are surface phenomena, they can be probed experimentally by Scanning Tunneling Microscopy (STM), a technique to observe the electronic structure of a material’s surface. Experiments at Princeton to examine these topological insulators and their surface states are underway. [4] In this independent work paper, we seek to perform a theoretical analysis of several physical phenomena involving the surface states of a topological insulator material when we apply certain impurity potentials at the surface, in the hopes that some of these results may be experimentally testable by STM experiments. In particular, the structure and phenomena investigated in this JP is as follows: we first introduce a simple model of a bulk topological insulator and exemplify how it differs from a trivial insulator; by exact diagonalization, of the system with a boundary, we show the presence of surface (edge) states, as well as their robustness to the application of edge impurities. We show by exactly diagonalizing the Hamiltonian that upon the application of time-reversal invariant impurity potentials (which we artificially maintain translationally invariant in one direction), the edge states remain robust. If the edge potential is increased, the edge reconstructs inside the material, by “flowing” around the

impurity. In the presence of small magnetic impurities, we show the surface state is destroyed entirely, and does not reconstruct into the bulk. We extend this analysis to provide a basis to perform similar calculations and simulations in the case of a three-dimensional (quasi-two dimensional) topological insulator. We then focus on the behavior of the edge modes in the presence a surface step-potential. These situations are directly related to experiments currently performed in the Yazdani group at Princeton. We adopt an effective action description in which we model the surface states of 3 dimensional topological insulators by 2-dimensional gapless Dirac fermions. We analyze the Klein tunneling of these fermions in barriers of geometries previously not analyzed in the literature. Trying to model the experiments, we derive the expression for the transmission coefficient with a single-barrier potential cited in [5] and then extend this problem to any *arbitrary* number of potential barriers. We perform this for different barrier geometries. Finally, we introduce hexagonal warping terms in our Dirac effective edge Hamiltonian, and suggest a way to re-analyze the tunneling problems in this setting. The hexagonal distortion terms are very important in the detailed physics of the Bi_2Te_3 insulator as they can lead to increased scattering.

2 A Two-Dimensional, Translation Invariant System: HgTe

In this section, we consider an inversion-symmetric, two-dimensional Hamiltonian for Mercury Telluride (HgTe), the first topological insulator discovered. We show the eigenvalue spectrum for this Hamiltonian and find the protected surface states. We also plot the localization profile of the wavefunctions on the edge of the material. We then add several additional terms to this Hamiltonian which break bulk inversion symmetry in the bulk of the material, and show that the surface states remain protected. We next add a scalar potential localized on the edge of the material and see that, upon increasing its value, the edge states reconstruct as to avoid the region of high scalar potential, but still remain gapless. Finally, we add edge terms which break time-reversal symmetry and examine their effects on the surface states. In this case, the terms open a gap in the edge states on the surface where they are placed and no reconstruction is observed.

Our HgTe model will be that of a two-dimensional (x,y) square lattice with two orbitals (s and p) per lattice site for each spin direction (spin up and spin down). We begin in section 2.1 by considering a simpler model (half of the HgTe model), known as the Chern insulator, where we do not consider spin and thus have only two, spatial orbitals per site. This model will have a Hall conductance and break Time-Reversal symmetry. The results obtained here are then easily extended to the standard HgTe Hamiltonian by “doubling” the spectrum in a way, described below, that restores time-reversal invariance.

2.1 Chern Insulator Hamiltonian

We start with a k -space Hamiltonian for the Chern insulator, periodic in both x and y directions, and transform this Hamiltonian into real space to impose non-periodic boundary conditions in the x -direction which give rise to the edge states. The simplest Hamiltonian is dictated by symmetry, as the coupling

between s and p orbitals has to be odd in momentum space[6]:

$$\mathcal{H} = \sum_k \begin{pmatrix} c_{1k}^\dagger & c_{2k}^\dagger \end{pmatrix} [A_1 \sin k_x \sigma_x + A_2 \sin k_y \sigma_y + (2 - M - \cos k_x - \cos k_y) \sigma_z] \begin{pmatrix} c_{1k} \\ c_{2k} \end{pmatrix} \quad (1)$$

where $c_{1k,2k}^\dagger$ and $c_{1k,2k}$ are creation and annihilation operators at orbitals 1, 2 of momentum k . A_1 , A_2 , and M are parameters which we set in our calculations, and σ_x , σ_y , σ_z are the $SU(2)$ matrices which in the current case act on orbital rather than spin space. As is traditional, we have left out the lattice constant, which has units of meters and multiplies k_x and k_y in the trig function terms, implicitly setting it equal to 1. We wish to diagonalize the Hamiltonian in a ‘‘Laughlin’’ cylinder geometry: we impose the non-periodic boundary condition in the x -direction so that \mathcal{H} is periodic in the y -direction and has L_x lattice sites in the x -direction. We now transform the Hamiltonian to real-space by taking term-by-term Fourier transforms. Keeping the k_y -dependence because k_y is still a good quantum number (as we are not attempting to modify the translational invariance of the Hamiltonian in this direction), we can write the k -space creation/annihilation operators as:

$$c_{\alpha,k} = \sum_j e^{ik_x j} c_{\alpha,k_y,j} \quad (2)$$

We first Fourier transform the terms in the Hamiltonian that do not depend on k_x , namely the $A_2 \sin k_y \sigma_y$ and $(2 - M - \cos k_y) \sigma_z$ terms:

$$\begin{aligned} A_2 \sin k_y \sigma_y + (2 - M - \cos k_y) \sigma_z &\longrightarrow \sum_j \begin{pmatrix} c_{1,k_y,j}^\dagger & c_{2,k_y,j}^\dagger \end{pmatrix} [A_2 \sin k_y \sigma_y + (2 - M - \cos k_y) \sigma_z] \begin{pmatrix} c_{1,k_y,j} \\ c_{2,k_y,j} \end{pmatrix} \\ &= \sum_j c_{\alpha,k_y,j}^\dagger \mathcal{U}_{\alpha\beta} c_{\beta,k_y,j} \end{aligned} \quad (3)$$

where repeated indices indicate summation and

$$\mathcal{U} = A_2 \sin k_y \begin{pmatrix} 0 & -i \\ i & 0 \end{pmatrix} + (2 - M - \cos k_y) \begin{pmatrix} 1 & 0 \\ 0 & -1 \end{pmatrix}$$

Next we look at the k_x -dependent terms, $A_1 \sin k_x \sigma_x$ and $-\cos k_x \sigma_z$. We have these terms in the Hamiltonian as

$$\mathcal{H}_{\sin k_x} = \sum_k \begin{pmatrix} c_{1k}^\dagger & c_{2k}^\dagger \end{pmatrix} [A_1 \sin k_x \sigma_x] \begin{pmatrix} c_{1k} \\ c_{2k} \end{pmatrix} \quad (4)$$

$$\mathcal{H}_{\cos k_x} = \sum_k \begin{pmatrix} c_{1k}^\dagger & c_{2k}^\dagger \end{pmatrix} [-\cos k_x \sigma_z] \begin{pmatrix} c_{1k} \\ c_{2k} \end{pmatrix} \quad (5)$$

Let’s start with the sine term (4) to manipulate it into the real-space representation:

$$\mathcal{H}_{\sin k_x} = \sum_k c_{\alpha k}^\dagger \mathcal{V}'_{\alpha\beta} \sin k_x c_{\beta k} = \sum_k c_{\alpha k}^\dagger \mathcal{V}'_{\alpha\beta} \left(\frac{e^{ik_x} - e^{-ik_x}}{2i} \right) c_{\beta k} = \sum_k c_{\alpha k}^\dagger \mathcal{V}_{\alpha\beta} \left(e^{ik_x} - e^{-ik_x} \right) c_{\beta k} \quad (6)$$

where

$$\mathcal{V} = \frac{\mathcal{V}'}{2i} = \frac{A_1}{2i} \begin{pmatrix} 0 & 1 \\ 1 & 0 \end{pmatrix}$$

We now recall our Fourier expansions for the creation and annihilation operators from equation (2) and plug them in to the two k_x -dependent terms of (6), e^{ik_x} and e^{-ik_x} :

$$\begin{aligned} \sum_k c_{\alpha k}^\dagger e^{ik_x} c_{\beta k} &= \sum_k \sum_{j_1} e^{-ik_x j_1} c_{\alpha, k_y, j_1}^\dagger e^{ik_x} \sum_{j_2} e^{ik_x j_2} c_{\beta, k_y, j_2} = \sum_{j_1, j_2} \delta_{j_1, j_2+1} c_{\alpha, k_y, j_1}^\dagger c_{\beta, k_y, j_2} \\ &= \sum_{j_2} c_{\alpha, k_y, j_2+1}^\dagger c_{\beta, k_y, j_2} \end{aligned} \quad (7)$$

where we've used the identity $\sum_k e^{ik_x(l-m)} = \delta_{l,m}$. Similarly, for the e^{-ik_x} term, we have:

$$\sum_k c_{\alpha k}^\dagger e^{-ik_x} c_{\beta k} = \sum_k \sum_{j_1} e^{-ik_x j_1} c_{\alpha, k_y, j_1}^\dagger e^{-ik_x} \sum_{j_2} e^{ik_x j_2} c_{\beta, k_y, j_2} = \sum_{j_2} c_{\alpha, k_y, j_2-1}^\dagger c_{\beta, k_y, j_2} \quad (8)$$

So putting these expressions (7) and (8) into (4) yields for the $A_1 \sin k_x \sigma_x$ term:

$$\mathcal{H}_{\sin k_x} = \sum_j \left(c_{\alpha, k_y, j+1}^\dagger \mathcal{V}_{\alpha\beta} c_{\beta, k_y, j} - c_{\alpha, k_y, j-1}^\dagger \mathcal{V}_{\alpha\beta} c_{\beta, k_y, j} \right) \quad (9)$$

We do the same thing for the $-\cos k_x \sigma_z$ term. From equation (5), we have:

$$\mathcal{H}_{\cos k_x} = - \sum_k c_{\alpha k}^\dagger \mathcal{T}'_{\alpha\beta} \cos k_x c_{\beta k} = - \sum_k c_{\alpha k}^\dagger \mathcal{T}_{\alpha\beta} \left(e^{ik_x} + e^{-ik_x} \right) c_{\beta k} \quad (10)$$

where

$$\mathcal{T} = \frac{1}{2} \begin{pmatrix} 1 & 0 \\ 0 & -1 \end{pmatrix}$$

Now using the expressions from equations (7) and (8), we obtain:

$$\mathcal{H}_{\cos k_x} = - \sum_j \left(c_{\alpha, k_y, j+1}^\dagger \mathcal{T}_{\alpha\beta} c_{\beta, k_y, j} + c_{\alpha, k_y, j-1}^\dagger \mathcal{T}_{\alpha\beta} c_{\beta, k_y, j} \right) \quad (11)$$

We now let $\mathcal{L}_{\alpha\beta} = \mathcal{V}_{\alpha\beta} - \mathcal{T}_{\alpha\beta}$ and $\mathcal{O}_{\alpha\beta} = \mathcal{V}_{\alpha\beta} + \mathcal{T}_{\alpha\beta}$, and combine equations (3), (9), and (11) to write our position space Hamiltonian as:

$$\mathcal{H}_{k_y} = \sum_j \left(c_{\alpha, k_y, j}^\dagger \mathcal{U}_{\alpha\beta} c_{\beta, k_y, j} + c_{\alpha, k_y, j+1}^\dagger \mathcal{L}_{\alpha\beta} c_{\beta, k_y, j} - c_{\alpha, k_y, j-1}^\dagger \mathcal{O}_{\alpha\beta} c_{\beta, k_y, j} \right) \quad (12)$$

We note that this Hamiltonian depends, still, on k_y , but our creation and annihilation operators act in position space to create these orbitals on the position-space square lattice. We are now in a position to apply this Hamiltonian to a position-space wavefunction and enforce the edge boundary condition in the x -direction. We thus want to solve the Schrodinger equation, $\mathcal{H}_{k_y} |\psi_{k_y}\rangle = E |\psi_{k_y}\rangle$, with the

single-particle states $|\psi_{k_y}\rangle$ given by

$$|\psi_{k_y}\rangle = \sum_{j,\theta} a_{\theta,k_y,j} c_{\theta,k_y,j}^\dagger |0\rangle$$

This wavefunction is a sum over lattice sites j and orbitals θ (here $j = 1 \rightarrow L_x$, $\theta = 1, 2$), where we create a particle on each site and orbital with creation operator $c_{\theta,k_y,j}^\dagger$. The amplitude of the wavefunction at each site/orbital is given by $a_{\theta,k_y,j}$. We of course retain the k_y dependence in all these terms, as the our Hamiltonian is for a given k_y . We recall the property of creation and annihilation operators:

$$c_{\beta,k_y,j_1} c_{\theta,k_y,j}^\dagger |0\rangle = \delta_{\theta\beta} \delta_{jj_1} |0\rangle \quad (13)$$

Now let's act on the wavefunction $|\psi_{k_y}\rangle$ with the Hamiltonian \mathcal{H}_{k_y} :

$$\begin{aligned} \mathcal{H}_{k_y} |\psi_{k_y}\rangle &= \left[\sum_j c_{\alpha,k_y,j}^\dagger \mathcal{U}_{\alpha\beta} c_{\beta,k_y,j} + c_{\alpha,k_y,j+1}^\dagger \mathcal{L}_{\alpha\beta} c_{\beta,k_y,j} - c_{\alpha,k_y,j-1}^\dagger \mathcal{O}_{\alpha\beta} c_{\beta,k_y,j} \right] \left[\sum_{j,\theta} a_{\theta,k_y,j} c_{\theta,k_y,j}^\dagger |0\rangle \right] \\ &= \left[\sum_j c_{\alpha,k_y,j}^\dagger \mathcal{U}_{\alpha\theta} a_{\theta,k_y,j} + c_{\alpha,k_y,j}^\dagger \mathcal{L}_{\alpha\theta} a_{\theta,k_y,j-1} - c_{\alpha,k_y,j}^\dagger \mathcal{O}_{\alpha\theta} a_{\theta,k_y,j+1} \right] |0\rangle \\ &= E \sum_{j,\theta} a_{\theta,k_y,j} c_{\theta,k_y,j}^\dagger |0\rangle \end{aligned}$$

We have made use of the relation (13) for creation and annihilation operators in the second line above, and adjusted indices. Since $c_{\theta,k_y,j}^\dagger |0\rangle$ are linearly independent, the Schrodinger equation reduces to j matrix equations:

$$\mathcal{U}_{\alpha\theta} a_{\theta j} + \mathcal{L}_{\alpha\theta} a_{\theta j-1} - \mathcal{O}_{\alpha\theta} a_{\theta j+1} = E a_{\theta j}$$

We can now apply the boundary condition in the x -direction such that we have an edge. Since j ranges from 1 to L_x , we set $a_{\theta 0} = a_{\theta L_x+1} = 0$, specifying that the wavefunction amplitudes on the sites just outside the square lattice are zero. This is in contrast with a periodic boundary condition in which we would have $a_{\theta L_x+1} = a_{\theta 1}$. The matrix equations therefore are:

$$\begin{aligned} \mathcal{U} \begin{pmatrix} a_{11} \\ a_{21} \end{pmatrix} - \mathcal{O} \begin{pmatrix} a_{12} \\ a_{22} \end{pmatrix} &= E \begin{pmatrix} a_{11} \\ a_{21} \end{pmatrix} \\ &\dots \\ \mathcal{U} \begin{pmatrix} a_{1j} \\ a_{2j} \end{pmatrix} + \mathcal{L} \begin{pmatrix} a_{1j-1} \\ a_{2j-1} \end{pmatrix} - \mathcal{O} \begin{pmatrix} a_{1j+1} \\ a_{2j+1} \end{pmatrix} &= E \begin{pmatrix} a_{1j} \\ a_{2j} \end{pmatrix} \\ &\dots \\ \mathcal{U} \begin{pmatrix} a_{1L_x} \\ a_{2L_x} \end{pmatrix} + \mathcal{L} \begin{pmatrix} a_{1L_x-1} \\ a_{2L_x-1} \end{pmatrix} &= E \begin{pmatrix} a_{1L_x} \\ a_{2L_x} \end{pmatrix} \end{aligned}$$

We form these equations into a $2L_x \times 2L_x$ matrix eigenvalue equation, with the matrix having \mathcal{U} on the

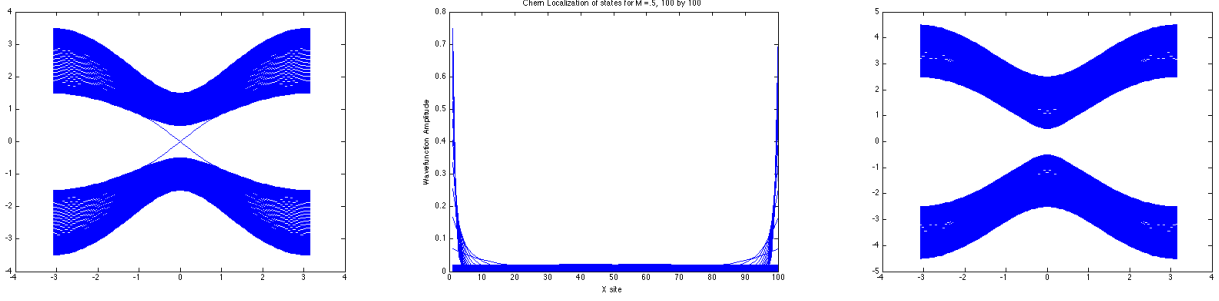


Figure 1: (Left) Plot of the eigenvalue spectrum, E versus k for 100 lattice sites with $M = 0.5$ for the Chern insulator. (Center) Wavefunction localization for the same system, showing the existence of edge modes localized on the edges of the lattice. (Right) Plot of the eigenvalue spectrum, E versus k for 100 lattice sites with $M = -0.5$ for the Chern insulator. We observe the phase transition between trivial and nontrivial topological classes at $M = 0$.

main diagonal, $-\mathcal{O}$ on the upper diagonal, \mathcal{L} on the lower diagonal, and zero elsewhere:

$$\begin{pmatrix} \mathcal{U} & -\mathcal{O} & 0 & \dots & 0 \\ \mathcal{L} & \mathcal{U} & -\mathcal{O} & \dots & 0 \\ 0 & \mathcal{L} & \mathcal{U} & \ddots & 0 \\ \vdots & \vdots & \ddots & \ddots & -\mathcal{O} \\ 0 & 0 & 0 & \mathcal{L} & \mathcal{U} \end{pmatrix} \begin{pmatrix} a_{12} \\ a_{22} \\ \vdots \\ a_{1L_x} \\ a_{2L_x} \end{pmatrix} = E \begin{pmatrix} a_{12} \\ a_{22} \\ \vdots \\ a_{1L_x} \\ a_{2L_x} \end{pmatrix} \quad (14)$$

For each k_y , we diagonalize to find eigenvectors and eigenvalues, and plot the eigenvalues for a $L_x = 100$ site lattice. For $A_1 = A_2 = 1$, and $M = 0.5$, we show plots of the eigenvalue spectrum and the localization of the wavefunctions in Figure 1. We can see the gapless edge modes (one mode on each edge) in the eigenvalue spectrum, and the localization plot (center), which charts the wavefunction amplitude over each lattice site in the x -direction, verifies that they are indeed located on left and right edges. There is a phase transition at $M = 0$ between a trivial and a nontrivial Chern insulator, as suggested in Figure 1, as the eigenvalue spectrum for $M = 0.5$ shows the gapless surface states and is thus of the nontrivial topology, whereas in the $M = -0.5$ spectrum, the surface states have vanished, and we have the trivial topology. The Chern insulator is an Integer Hall effect without applied magnetic field, but with a lattice time-reversal symmetry breaking term.

2.2 2D Quantum Spin Hall Hamiltonian: HgTe

Though the matrix equations we derived in the previous section applied to the simpler, Chern insulator Hamiltonian, in which we ignored spin, we can readily extend this prescription to a system with spin, by letting θ run over 4 different orbitals (s and p for both spin up and spin down). In essence, this “quantum spin hall” Hamiltonian for HgTe consists of two copies of the Chern insulator Hamiltonian, one with spin up and one with spin down. It is called the quantum spin hall (QSH) Hamiltonian because the system can be seen as two copies of the integer quantum hall effect, with spins traveling in the opposite directions around the material, so that there is no net charge quantum Hall conductance (as equal numbers of spin up and spin down electrons are traveling in opposite directions), but the Hall

conductivity of the spins is quantized. If we let our original Chern insulator Hamiltonian be denoted $h(k)$, then the QSH Hamiltonian which, unlike the Chern insulator, respects time-reversal invariance, is given by:

$$H(k) = \begin{pmatrix} h(k) & 0 \\ 0 & h^T(-k) \end{pmatrix} \quad (15)$$

To see why this must be true, we consider a general system with spin up and down given by the Hamiltonian

$$H(k) = \begin{bmatrix} h_{\uparrow\uparrow}(k) & h_{\uparrow\downarrow}(k) \\ h_{\downarrow\uparrow}(k) & h_{\downarrow\downarrow}(k) \end{bmatrix} \quad (16)$$

and apply the time reversal operator defined by $T = -i\sigma_y K$, where K is the operator for complex conjugation:

$$TH(k)T^{-1} = \sigma_y H^*(k) \sigma_y = \sigma_y H^T(k) \sigma_y = \begin{bmatrix} h_{\downarrow\downarrow}^T(k) & -h_{\uparrow\downarrow}^T(k) \\ -h_{\downarrow\uparrow}^T(k) & h_{\uparrow\uparrow}^T(k) \end{bmatrix} \quad (17)$$

where the first equality follows from $\sigma_y^{-1} = \sigma_y$, and the second since H is Hermitian. Since the system obeys time-reversal invariance, $TH(k)T^{-1} = H(-k)$ (as the time reversal operator sends k to $-k$), and we can equate the H_{11} elements of (17) and (16) to obtain $h_{\downarrow\downarrow}(k) = h_{\uparrow\uparrow}^T(-k)$ and thus the Hamiltonian in (15). For the QSH model then, we simply replace the Pauli matrices with Γ_1 , Γ_2 , and Γ_3 from [6] respectively and consider θ from 1 to 4. To see this more explicitly, we look at these Γ_i matrices:

$$\Gamma_1 = \begin{pmatrix} 0 & 1 & 0 & 0 \\ 1 & 0 & 0 & 0 \\ 0 & 0 & 0 & -1 \\ 0 & 0 & -1 & 0 \end{pmatrix}, \quad \Gamma_2 = \begin{pmatrix} 0 & -i & 0 & 0 \\ i & 0 & 0 & 0 \\ 0 & 0 & 0 & -i \\ 0 & 0 & i & 0 \end{pmatrix}, \quad \Gamma_3 = \begin{pmatrix} 1 & 0 & 0 & 0 \\ 0 & -1 & 0 & 0 \\ 0 & 0 & 1 & 0 \\ 0 & 0 & 0 & -1 \end{pmatrix}$$

and note that in our Hamiltonian, modified from equation (1), Γ_1 and Γ_2 , replacing σ_x and σ_y , respectively, multiply terms odd in k , namely $\sin k_x$ and $\sin k_y$, whereas Γ_3 , replacing σ_z , multiplies only terms even in k . Thus we verify that the condition $h_{\downarrow\downarrow}(k) = h_{\uparrow\uparrow}^T(-k)$ holds for this QSH Hamiltonian by noting that for Γ_1 and Γ_2 , the lower diagonal block equals the negative transpose of the upper diagonal block, whereas for Γ_3 , the lower diagonal block equals the transpose of the upper diagonal block. This minus sign is precisely accounted for in the terms odd in k when we send k to $-k$ to satisfy this condition. Thus we have restored time-reversal invariance. The eigenvalue spectrum and edge localizations here are the same as in the Chern insulator case, except there are two copies of each edge mode.

2.3 Inversion Symmetry-Breaking Terms

In this section, we add terms which break inversion symmetry in the bulk to our Hamiltonian and see that the surface states are robust to this symmetry breaking. The terms we wish to add to our Hamiltonian

are the following:

$$\Gamma_{35} = \begin{pmatrix} 0 & 0 & 0 & -1 \\ 0 & 0 & 1 & 0 \\ 0 & 1 & 0 & 0 \\ -1 & 0 & 0 & 0 \end{pmatrix}, \quad \Gamma_{34} = \begin{pmatrix} 0 & 0 & 0 & i \\ 0 & 0 & -i & 0 \\ 0 & i & 0 & 0 \\ -i & 0 & 0 & 0 \end{pmatrix}, \quad \Gamma_{23} = \begin{pmatrix} 0 & -1 & 0 & 0 \\ -1 & 0 & 0 & 0 \\ 0 & 0 & 0 & -1 \\ 0 & 0 & -1 & 0 \end{pmatrix}, \quad \Gamma_{13} = \begin{pmatrix} 0 & -i & 0 & 0 \\ i & 0 & 0 & 0 \\ 0 & 0 & 0 & i \\ 0 & 0 & -i & 0 \end{pmatrix}$$

To see that they break inversion symmetry, we consider the inversion matrix P for this system: $P = \Gamma_3$, defined as such so that it sends the two-orbital, two-spin wavevector $\psi = [|s, \uparrow\rangle, |p, \uparrow\rangle, |s, \downarrow\rangle, |p, \downarrow\rangle]$ to $[|s, \uparrow\rangle, -|p, \uparrow\rangle, |s, \downarrow\rangle, -|p, \downarrow\rangle]$. That is, the p orbitals are odd under a parity (inversion) transformation, and the s orbitals are even—a basic fact from quantum mechanics and the shape of the s and p orbitals (s is spherically symmetric). Having determined our inversion matrix, we can readily see that for all the Γ matrices listed just above, $P\Gamma P^{-1} = -\Gamma$, and inversion symmetry in the Hamiltonian is therefore broken, as the parity operator no longer leaves the system invariant.

By a similar prescription to that described for the parity operator, one can also show that these matrices are all time-reversal invariant. Thus we expect that the surface states in HgTe are robust in the presence of these inversion-breaking terms. Rediagonalizing our Hamiltonian with these additional terms (one at a time) yields the spectra shown in Figure 2. We see that for each additional term, the spectrum remains gapless. The broken inversion symmetry may cause the two copies of the edge modes to no longer be identical, as for Γ_{13} , but this corresponds, as we see, only to shift in the spectrum and not an opening of a gap. As we increase the weight Δ by which we multiply the Γ term, we see that the bulk gap begins to close, maintaining the surface states. Once the bulk gap closes, for values of $\Delta \approx 0.9$ in our calculations, it opens back up without any surface states, representing a phase transition between the topologically nontrivial and topologically trivial classes.

2.4 Surface Impurities

Whereas in the previous section, we added these inversion-breaking impurities throughout the material, in this section we concentrate on what happens to the edge states when we place an additional impurity potential term on the edge. In Figure 3, we have added a constant scalar potential $V = 0.3$ to the last two lattice sites. In the spectrum plot (center), we see that one of the surface states, corresponding to the edge mode on the edge on which we’ve applied the potential, shifts upward by the amount of the applied potential. We note, of course, that both edge modes remain gapless. Furthermore, we can see the edge mode receding into the bulk in the presence of this surface impurity from the plots of the wavefunction amplitudes. On the left, we observe this effect of the surface state “flowing around” the potential impurity for $V = 0.3$. On the right, the effect becomes more pronounced as we increase the scalar potential on the edge to $V = 1.5$.

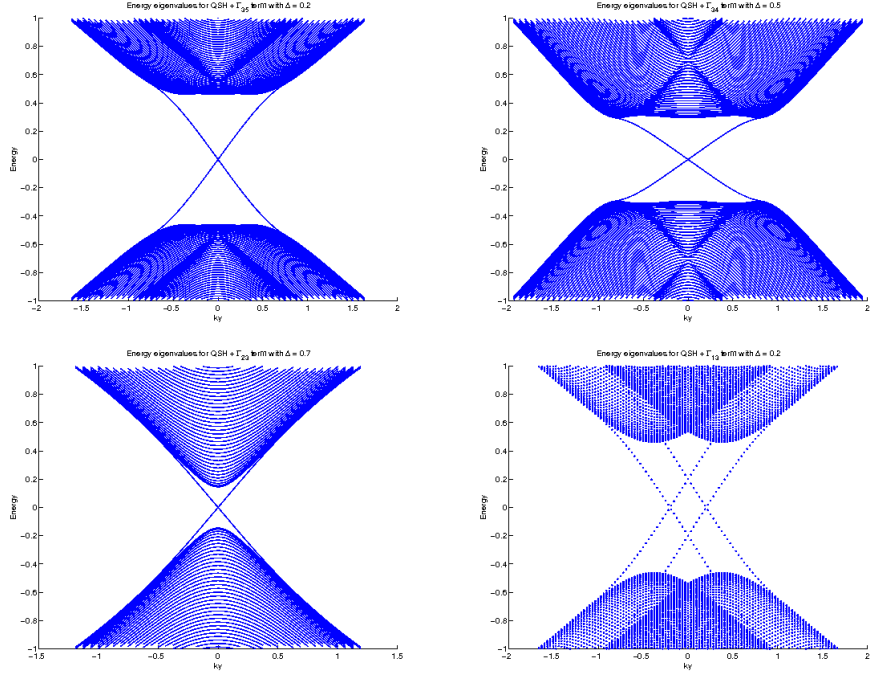


Figure 2: Plots of E versus k , the eigenvalue spectra for 100 lattice sites with $M = -0.5$ for different inversion breaking terms and weights Δ . The upper left plot was obtained by adding the Γ_{35} term with weight $\Delta = 0.2$; the upper right, Γ_{34} with weight $\Delta = 0.5$; the lower left, Γ_{23} with weight $\Delta = 0.7$; and the lower right, Γ_{13} with weight $\Delta = 0.2$

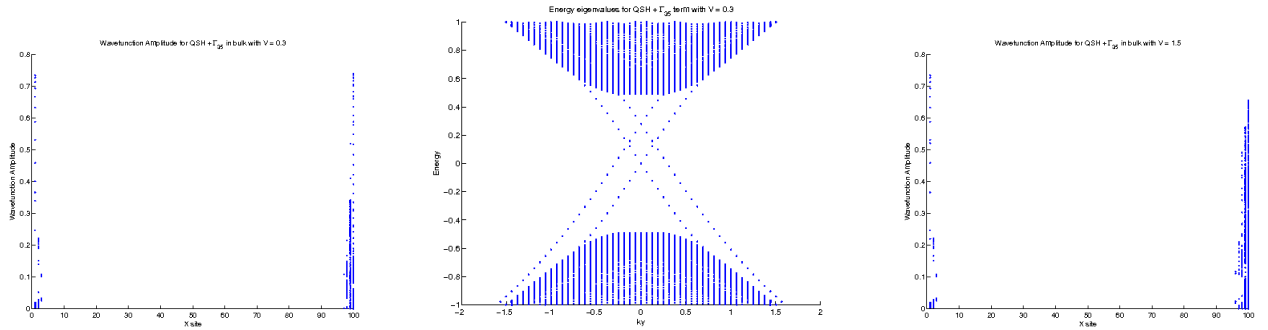


Figure 3: Plots for Γ_{35} in the bulk and a scalar potential V on the edge. The surface states are shifted upwards from the potential (center, $V = 0.3$) and they recede into the bulk. On the left, we have $V = 0.3$ and see the recession into the bulk beginning. On the right, $V = 1.5$, and we see this effect becoming more pronounced.

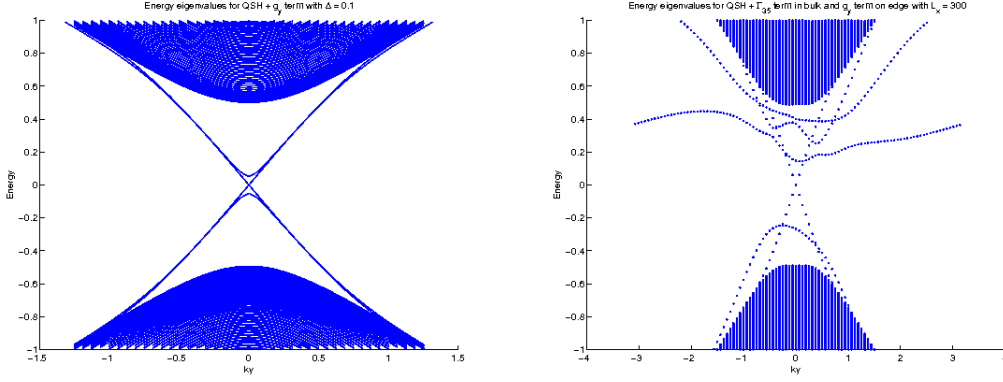


Figure 4: (Left) Energy eigenvalue spectrum for TR-breaking term g_y on the last 5 lattice sites. (Right) Eigenvalue spectrum with the g_y TR-breaking term added onto the last 2 lattice sites and Γ_{35} in the bulk for $L_x = 300$.

Finally, we introduce a time-reversal breaking impurity term into our system,

$$g_y = \begin{pmatrix} 0 & 0 & -i & 0 \\ 0 & 0 & 0 & 0 \\ i & 0 & 0 & 0 \\ 0 & 0 & 0 & 0 \end{pmatrix}$$

In Figure 4, on the left we show the eigenvalue spectrum when we place this term on the last 5 lattice sites. We see that a gap opens in one of the edge modes (on which we've placed this impurity potential), as time-reversal is broken there, while the other edge mode (on the other edge of the lattice) is unaffected by this local impurity. On the right of Figure 4, we have placed this g_y term on the last two lattice sites, in addition to the inversion breaking Γ_{35} term throughout the lattice. We see a large gap opens up, destroying the surface state on which we have placed the magnetic impurity term. We also varied L_x , the number of sites in the x -direction of the lattice, but the large gap persisted and there was no evidence of any reconstruction of the edge states in the bulk. The spectrum shown here is taken for $L_x = 300$, whereas all other plots in these sections were for a lattice size of $L_x = 100$. As the gap persists even as we increase L_x , we thus conclude that the edge modes do not reconstruct, but are destroyed in the presence of a time-reversal breaking impurity.

2.5 Extension 3D Topological Insulators

Finally, before leaving the tight binding model Hamiltonian for Dirac surface states, we extend the previous analysis to the possibility of considering three-dimensional Hamiltonians. Again, this is a quasi-2D picture, as for the third dimension we employ periodic boundary conditions. We show here in Figure 5 cuts similar to the 2D cuts displaying the surface states shown above. As we can see though, instead of an X-like shape, involving two surface bands, we have an entire Dirac cone in this case. This Dirac cone is of much current experimental interest for its ability to host exotic states of matter such as an anomalous quantum hall state, Majorana fermions, or magnetic monopoles, when put into interaction with other ordered phases of matter such as magnetism or superconductivity.

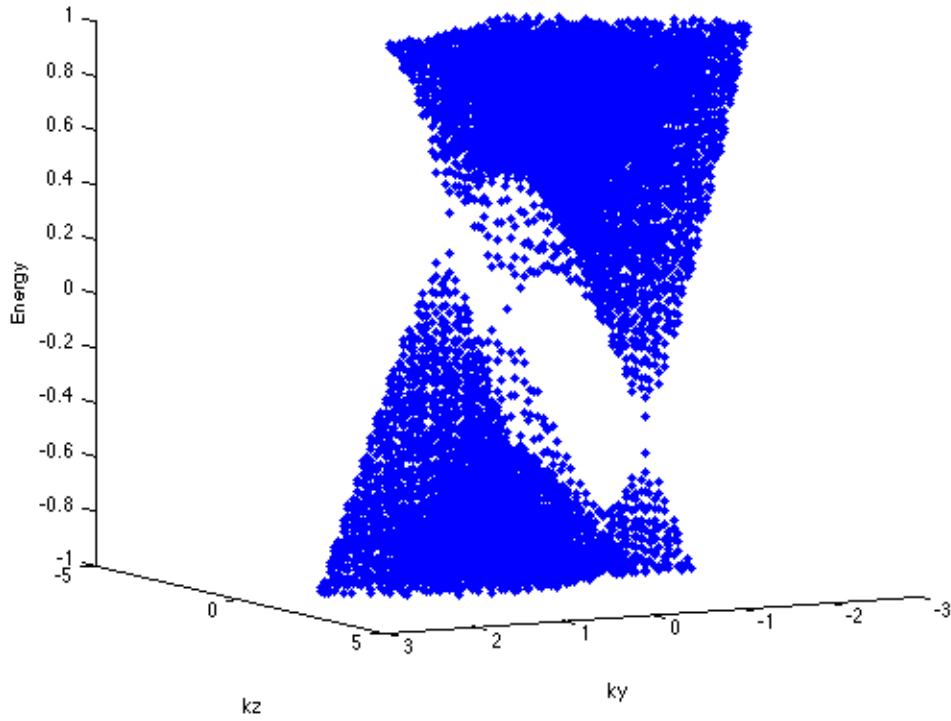
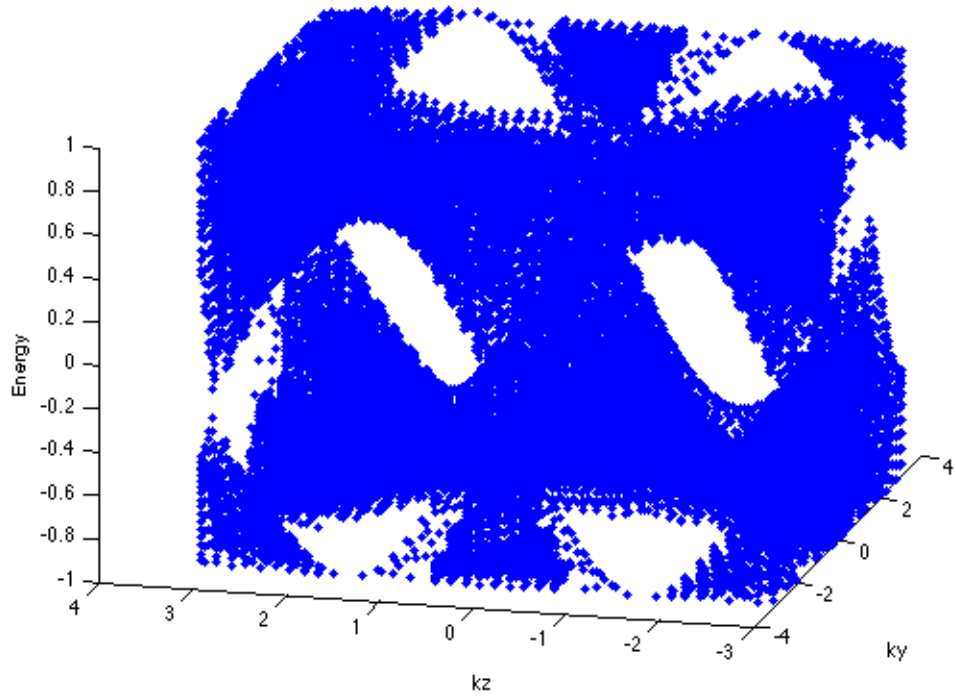


Figure 5: Plots of Energy as a function of k_z and k_y for the three-dimensional topological insulator case. The second figure is a smaller segment of the first for the sake of visibility of the Dirac cones.

3 Potential Barriers on 3D Topological Insulators without Translational Invariance

Having examined the question of edge reconstruction on the edges of a two-dimensional, translationally invariant topological insulator, we now turn our attention to the physics of surface states of the *three-dimensional* strong topological insulators. These insulators exhibit topologically protected surface states very much like their two-dimensional siblings studied in the previous sections. However, the surface states are now two-dimensional, and they are described, at low energies, by the two-dimensional Dirac Hamiltonian (presented below). We add to the surface of the topological insulator a step barrier potential which simulates the atomic layer-thick step-ridges present on the surface of Bi₂Te₃ (as observed by experiments in the Yazdani group). We place potential impurities in the form of barriers on this surface and calculate the transmission coefficients for Dirac fermions scattering off these impurity barriers.

4 The Klein Tunneling Problem

In this section, we derive the results in [5] as a starting point for our examination of transmission through potential barriers for a Dirac Hamiltonian. We consider a single potential barrier of height V_0 , solve the Schrodinger equation for the Dirac Hamiltonian, and apply boundary conditions in different potential regions to obtain the transmission coefficient of a Dirac fermion through the barrier.

4.1 Verifying the Ansatz: Finding k_x , k_y , q_x , and θ

We begin with the Dirac-like Hamiltonian,

$$H_0 = -i\hbar v_F \sigma \nabla \tag{18}$$

and potential

$$V(x) = \begin{cases} V_0, & 0 < x < D, \\ 0, & \text{otherwise} \end{cases} \tag{19}$$

which give us the Schrodinger equation in the Dirac spinor basis:

$$-i\hbar v_F \begin{pmatrix} 0 & -i\partial_y + \partial_x \\ i\partial_y + \partial_x & 0 \end{pmatrix} \begin{pmatrix} \psi_1 \\ \psi_2 \end{pmatrix} + V(x) \begin{pmatrix} \psi_1 \\ \psi_2 \end{pmatrix} = E \begin{pmatrix} \psi_1 \\ \psi_2 \end{pmatrix}. \tag{20}$$

We now look at our ansatz from [5], which we wish to plug into (20) to find conditions on k_x , k_y , q_x , and θ :

$$\begin{aligned} \psi_1(x, y) &= \begin{cases} (e^{ik_x x} + r e^{-ik_x x}) e^{ik_y y}, & x < 0, \\ (a_1 e^{iq_x x} + b_1 e^{-iq_x x}) e^{ik_y y}, & 0 < x < D, \\ t e^{ik_x x + ik_y y}, & x > D \end{cases} \\ \psi_2(x, y) &= \begin{cases} s(e^{ik_x x + i\phi} - r e^{-ik_x x - i\phi}) e^{ik_y y}, & x < 0 \\ s'(a_1 e^{iq_x x + i\theta} - b_1 e^{-iq_x x - i\theta}) e^{ik_y y}, & 0 < x < D \\ s t e^{ik_x x + ik_y y + i\phi}, & x > D \end{cases} \end{aligned}$$

We notice that all y-dependence is in the form $e^{ik_y y}$, so we can replace $\partial_y \psi$ with $ik_y \psi$ everywhere. In the region $x < 0$, $V(x) = 0$, and the Schrodinger equation yields two equations in ψ_1 and ψ_2 :

$$-ik_y \psi_2 - i\partial_x \psi_2 = \frac{E}{\hbar v_F} \psi_1 \quad \text{and} \quad ik_y \psi_1 - i\partial_x \psi_1 = \frac{E}{\hbar v_F} \psi_2 \quad (21)$$

Now, let's plug in ψ_1 and ψ_2 from the ansatz into the first half of equation (21):

$$\begin{aligned} \frac{E}{\hbar v_F} (e^{ik_x x} + r e^{-ik_x x}) &= -ik_y s (e^{ik_x x + i\phi} - r e^{-ik_x x - i\phi}) + s k_x (e^{ik_x x + i\phi} + r (e^{-ik_x x - i\phi})) \\ &= s e^{ik_x x + i\phi} (k_x - ik_y) + s r e^{-ik_x x - i\phi} (k_x + ik_y) \end{aligned}$$

Rearranging yields

$$e^{ik_x x} \left(s e^{i\phi} (k_x - ik_y) - \frac{E}{\hbar v_F} \right) + r e^{-ik_x x} \left(s e^{-i\phi} (k_x + ik_y) - \frac{E}{\hbar v_F} \right) = 0$$

Since $e^{ik_x x}$ and $e^{-ik_x x}$ are linearly independent and the expression is 0 for all x , their coefficients are each equal to 0:

$$k_x - ik_y = k_F e^{-i\phi} \quad \text{and} \quad k_x + ik_y = k_F e^{i\phi} \quad (22)$$

where, recalling that $s = \text{sgn}(E)$ (additionally, $s' = \text{sgn}(E - V_0)$), we define

$$k_F = \frac{E}{s \hbar v_F} = \frac{|E|}{\hbar v_F}$$

Adding equations (22) together gives a condition for k_x and subtracting them gives a condition for k_y :

$$k_x = k_F \cos \phi \quad \text{and} \quad k_y = k_F \sin \phi \quad (23)$$

Though we do not show it here, if we plug ψ_1 and ψ_2 into the second half of equation (21) instead, we obtain the exact same expressions for k_y and k_x . Now, we consider the region $0 < x < D$, where $V(x) = V_0$ and our Schrodinger equation yields again two equations in ψ_1 and ψ_2 . Making the same substitution of $ik_y \psi$ for $\partial_y \psi$ yields:

$$-ik_y \psi_2 - i\partial_x \psi_2 = \frac{E - V_0}{\hbar v_F} \psi_1 \quad \text{and} \quad ik_y \psi_1 - i\partial_x \psi_1 = \frac{E - V_0}{\hbar v_F} \psi_2. \quad (24)$$

Again, we plug expressions for ψ_1 and ψ_2 from the ansatz, this time in the region $0 < x < D$ into the first part of equation (24) and define $k'_F = \frac{E - V_0}{\hbar v_F}$

$$-ik_y s' (a_1 e^{iq_x x + i\theta} - b_1 e^{-iq_x x - i\theta}) + s' q_x (a_1 e^{iq_x x + i\theta} + b_1 (e^{-iq_x x - i\theta})) = k'_F (a_1 e^{iq_x x} + b_1 e^{-iq_x x}) \quad (25)$$

Rearranging gives

$$e^{iq_x x} \left(a_1 s' e^{i\phi} (q_x - ik_y) - a_1 k'_F \right) + e^{-iq_x x} \left(b_1 s' e^{-i\theta} (q_x + ik_y) - b_1 k'_F \right) = 0$$

Again exploiting the linear independence of $e^{iq_x x}$ and $e^{-iq_x x}$ we find that their coefficients equal 0,

yielding

$$q_x - ik_y = \frac{k'_F}{s'} e^{-i\theta} \quad \text{and} \quad q_x + ik_y = \frac{k'_F}{s'} e^{i\theta} \quad (26)$$

Adding equations (26) gives a condition for q_x and subtracting them gives a condition for k_y in terms of θ :

$$q_x = \frac{k'_F}{s'} \cos \theta \quad \text{and} \quad k_y = \frac{k'_F}{s'} \sin \theta$$

so that dividing the two conditions yields an expression for θ :

$$\tan \theta = \frac{k_y}{q_x} \quad (27)$$

and expanding our expression for q_x yields:

$$q_x = \frac{k'_F}{s'} \cos \theta = \frac{k'_F}{s'} \sqrt{1 - \sin^2 \theta} = \sqrt{\left(\frac{k'_F}{s'}\right)^2 - \left(\frac{k'_F}{s'}\right)^2 \sin^2 \theta} = \sqrt{\left(\frac{E - V_0}{\hbar v_F}\right)^2 - k_y^2} \quad (28)$$

We have now obtained all the relations between k_x , k_y , q_x , θ , and ϕ stated in [5]. In the next section, we apply the boundary conditions and obtain an expression for the transmission coefficient.

4.2 Applying the Boundary Conditions: Finding r

We now return to our ansatz and apply the boundary conditions that ψ_1 and ψ_2 are continuous at $x = 0$ and $x = D$. This conditions yield the system of 4 equations in 4 unknowns (a, b, r, t):

$$a_1 + b_1 = r + 1 \quad (29)$$

$$te^{ik_x D} = a_1 e^{iq_x D} + b_1 e^{-iq_x D} \quad (30)$$

$$s(e^{i\phi} - re^{-i\phi}) = s'(a_1 e^{i\theta} - b_1 e^{-i\theta}) \quad (31)$$

$$s'(a_1 e^{iq_x D + i\theta} - b_1 e^{-iq_x D - i\theta}) = ste^{ik_x D + i\phi} \quad (32)$$

We begin by dividing equation (32) by equation (30):

$$se^{i\phi} = \frac{s'(a_1 e^{iq_x D + i\theta} - b_1 e^{-iq_x D - i\theta})}{a_1 e^{iq_x D} + b_1 e^{-iq_x D}}$$

Rearranging and solving for b_1 in terms of a_1 yields:

$$b_1 = -a_1 e^{2iq_x D} \left(\frac{se^{i\phi} - s'e^{i\theta}}{se^{i\phi} + s'e^{-i\theta}} \right) \quad (33)$$

Next, we plug (29) in the form of $r = a_1 + b_1 - 1$ into (31):

$$s(e^{i\phi} - (a_1 + b_1 - 1)e^{-i\phi}) = s'(a_1 e^{i\theta} - b_1 e^{-i\theta})$$

Rearranging, we get:

$$a_1(s'e^{i\theta} + se^{-i\phi}) = b_1(s'e^{-i\theta} - se^{-i\phi}) + 2s \cos \phi \quad (34)$$

We now plug equation (33) into equation (34):

$$\begin{aligned} a_1(s'e^{i\theta} + se^{-i\phi}) &= 2s \cos \phi - a_1 e^{2iq_x D} \left(\frac{se^{i\phi} - s'e^{i\theta}}{se^{i\phi} + s'e^{-i\theta}} \right) (s'e^{-i\theta} - se^{-i\phi}) \\ &= 2s \cos \phi - a_1 e^{2iq_x D} \left(\frac{2ss' \cos(\phi - \theta) - 2}{se^{i\phi} + s'e^{-i\theta}} \right) \end{aligned}$$

Rearranging and simplifying,

$$\begin{aligned} 2s \cos \phi &= a_1 \left[s'e^{i\theta} + se^{-i\phi} + e^{2iq_x D} \left(\frac{2ss' \cos(\phi - \theta) - 2}{se^{i\phi} + s'e^{-i\theta}} \right) \right] \\ &= a_1 \left[\frac{2 + ss'e^{i(\phi+\theta)} + ss'e^{-i(\phi+\theta)} + 2e^{2iq_x D} (ss' \cos(\phi - \theta) - 1)}{se^{i\phi} + s'e^{-i\theta}} \right] \\ &= a_1 \left[\frac{2ss'[\cos(\phi + \theta) + e^{2iq_x D} \cos(\phi - \theta)] - 4ie^{iq_x D} \sin(q_x D)}{se^{i\phi} + s'e^{-i\theta}} \right] \end{aligned}$$

So we obtain an expression for a_1 :

$$a_1 = \frac{s \cos \phi (se^{i\phi} + s'e^{-i\theta}) e^{-iq_x D}}{ss'[e^{-iq_x D} \cos(\phi + \theta) + e^{iq_x D} \cos(\phi - \theta)] - 2i \sin(q_x D)} \quad (35)$$

Now we plug a_1 , equation (35), into our expression for b_1 , equation (33) to obtain:

$$b_1 = -\frac{s \cos \phi (se^{i\phi} - s'e^{i\theta}) e^{iq_x D}}{ss'[e^{-iq_x D} \cos(\phi + \theta) + e^{iq_x D} \cos(\phi - \theta)] - 2i \sin(q_x D)} \quad (36)$$

We note that the denominator is the same as that in the expression for r in [5], so we will not modify it, and thus denote it by “denom” in the next few steps. To obtain r , we plug our expressions for a and b into equation (29):

$$r = a_1 + b_1 - 1 = \frac{s \cos \phi (se^{i\phi} + s'e^{-i\theta}) e^{-iq_x D} - s \cos \phi (se^{i\phi} - s'e^{i\theta}) e^{iq_x D} - \text{denom}}{\text{denom}} = \frac{\text{num}}{\text{denom}}$$

We've introduced “num” to refer to the numerator of r , and we now simplify this expression:

$$\begin{aligned} \text{num} &= s \cos \phi [s'e^{-i(\theta+q_x D)} + s'e^{i(\theta+q_x D)} - 2ise^{i\phi} \sin(q_x D)] \\ &\quad - ss'[e^{-iq_x D} \cos(\phi + \theta) + e^{iq_x D} \cos(\phi - \theta)] + 2i \sin(q_x D) \\ &= -2ss' \sin \theta \sin(q_x D) (\cos \phi + \sin \phi) + 2 \sin \phi \sin(q_x D) (\cos \phi + i \sin \phi) \\ &= 2e^{i\phi} \sin(q_x D) (\sin \phi - ss' \sin \theta) \end{aligned}$$

So finally, we arrive at an expression for r , which differs from the equation in [5] by an overall factor of i :

$$r = 2e^{i\phi} \sin(q_x D) \times \frac{\sin \phi - ss' \sin \theta}{ss'[e^{-iq_x D} \cos(\phi + \theta) + e^{iq_x D} \cos(\phi - \theta)] - 2i \sin(q_x D)} \quad (37)$$

4.3 Transmission Coefficient for $|V_0| \gg |E|$

In the limit of $|V_0| \gg |E|$, we have the following simplifications:

$$\begin{aligned} q_x &\approx \sqrt{\left(\frac{V_0}{\hbar v_F}\right)^2 - \left(\frac{V_0}{\hbar v_F}\right)^2 \sin^2 \phi} \approx \left|\frac{V_0}{\hbar v_F}\right| \\ \theta &\approx \frac{k_y}{|V_0/\hbar v_F|} \approx \left|\frac{E}{V_0}\right| \sin \phi \ll 1 \\ \sin \theta &\approx \theta \\ \cos \theta &\approx 1 \end{aligned}$$

Let's write the numerator and denominator of r using these $|V_0| \gg |E|$ approximations:

$$\begin{aligned} \text{num} &\approx 2e^{i\phi} \sin(q_x D) (\sin \phi - ss' \left|\frac{E}{V_0}\right| \sin \phi) \\ &\approx 2e^{i\phi} \sin(q_x D) \sin \phi \end{aligned}$$

$$\begin{aligned} \text{denom} &\approx ss' [e^{-iq_x D} \cos \phi + e^{iq_x D} \cos \phi] - 2i \sin(q_x D) \\ &\approx 2ss' [\cos \phi \cos(q_x D)] - 2i \sin(q_x D) \end{aligned}$$

Combining these and multiplying r by complex conjugate r^* yields, in the limit of $|V_0| \gg |E|$:

$$|r|^2 = \frac{\sin^2(q_x D) \sin^2 \phi}{\cos^2 \phi \cos^2(q_x D) + \sin^2(q_x D)}$$

So the transmission coefficient T is given by:

$$\begin{aligned} T = 1 - |r|^2 &= \frac{\cos^2 \phi \cos^2(q_x D) + \sin^2(q_x D)(1 - \sin^2 \phi)}{\cos^2 \phi \cos^2(q_x D) - \cos^2(q_x D) + \sin^2(q_x D) + \cos^2(q_x D)} \\ &= \frac{\cos^2 \phi}{1 - \sin^2 \phi \cos^2(q_x D)} \end{aligned}$$

We see that for $q_x D = n\pi$, $T = 1$ and we have perfect transmission through the barrier. Additionally, we have this perfect transmission for $\phi = 0$. This is the result cited in [5]. In Figure 6, we reproduce the results from [5], plotting T as a function of incident angle ϕ for two specific energy E and barrier height V_0 combinations. In Figure 7 and Figure 8, below, we show plots of the transmission coefficient (without taking the large V_0 limit) as a function of incident angle ϕ and barrier height V_0 at different energies.

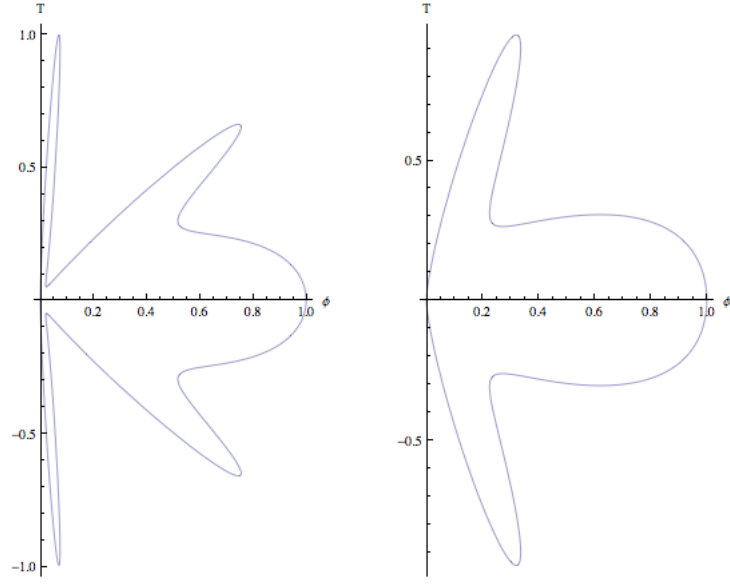


Figure 6: Polar plots of transmission coefficients as a function of incident angle ϕ for barrier heights of $V_0 = 200$ meV and 285 meV, and energy $E = 83.25$ meV.

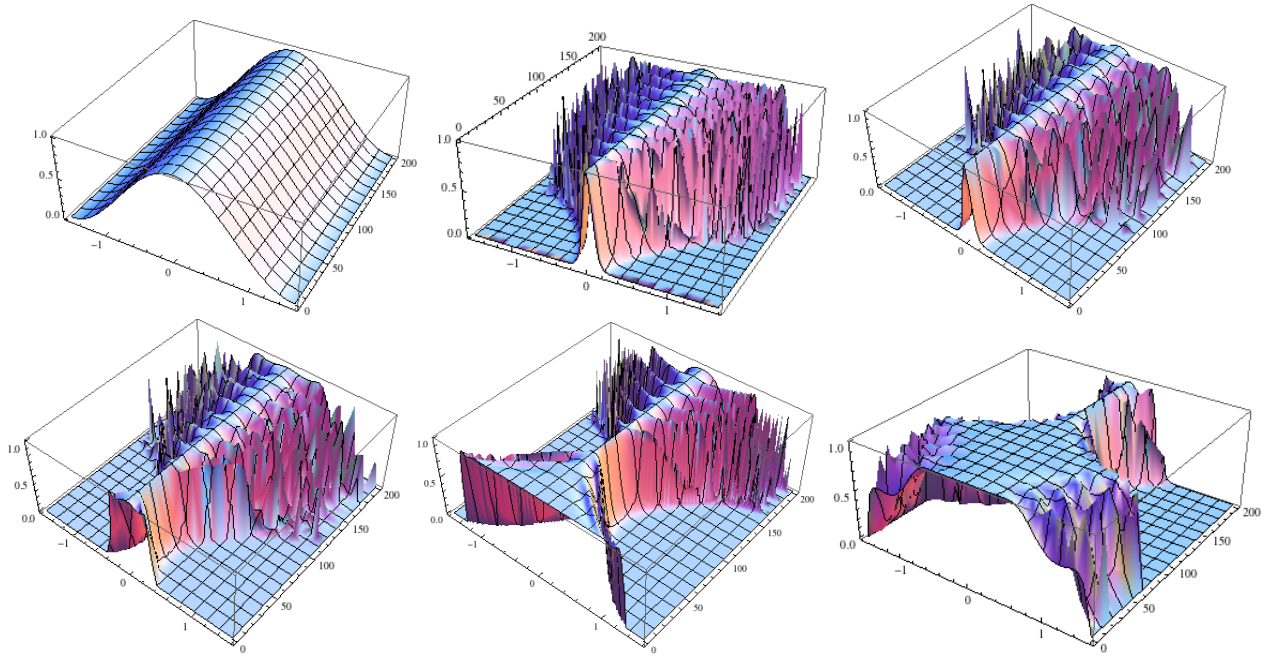


Figure 7: 3D plots of transmission coefficients as a function of incident angle ϕ and barrier height V_0 for energies $E = 0.0001, 5, 30, 80,$ and 150 . V_0 ranges from 0 to 200 meV and ϕ from $-\pi/2$ to $\pi/2$.

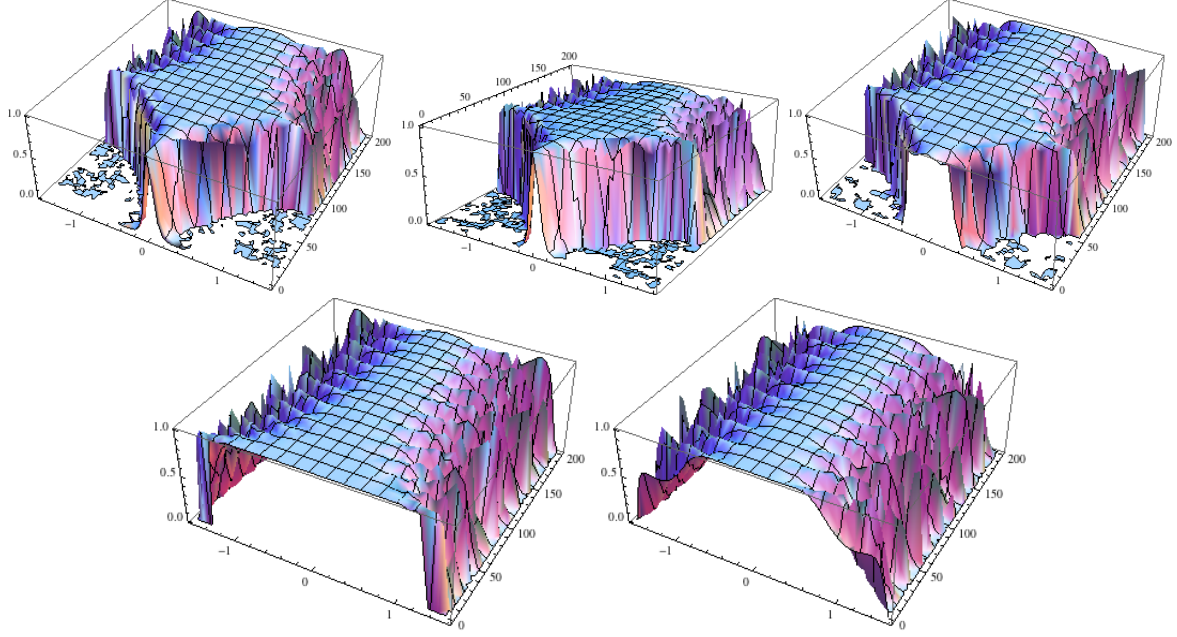


Figure 8: 3D plots of transmission coefficients as a function of incident angle ϕ and barrier height V_0 for energies $E = 0, -0.0001, -5, -30, -80, \text{ and } -150$. Again, V_0 ranges from 0 to 200 meV and ϕ from $-\pi/2$ to $\pi/2$.

5 Hexagonal Warping: The k^3 Hamiltonian for Bi_2Te_3

5.1 Single Barrier, Height V_0 , Along ΓK

5.1.1 Outside the Barrier, $x < 0$

Finally, we wish to turn our attention to a recently suggested additional term in the Hamiltonian for Bi_2Te_3 . Motivated by Angle-Resolved Photoemission Spectroscopy (ARPES) experiments on the 3D strong topological insulator Bi_2Te_3 , which showed a snow-flake like Fermi surface, hexagonally distorted, Fu has suggested that this distortion is due to an additional term in the Hamiltonian proportional to k^3 . Thus the entire Hamiltonian for Bi_2Te_3 has the form[7]:

$$H(\vec{k}) = v(k_x\sigma_y - k_y\sigma_x) + \frac{\lambda}{2}(k_+^3 + k_-^3)\sigma_z \quad (38)$$

where $k_{\pm} = k_x \pm ik_y$. To see this ‘‘hexagonal warping’’ of the Fermi surface, we derive a relation between E and k . We proceed as in Section 4, writing the Schrodinger equation with this new Hamiltonian operating on the Dirac spinor wavefunctions and applying it to a suitable ansatz. We start by rewriting the k^3 term in the Hamiltonian in terms of k_x and k_y , so that we can transform them into position space as before:

$$k_+^3 + k_-^3 = (k_x + ik_y)^3 + (k_x - ik_y)^3 = 2k_x^3 - 6k_y^2k_x$$

so that our Hamiltonian becomes

$$H(\vec{k}) = v(k_x\sigma_y - k_y\sigma_x) + \lambda(k_x^3 - 3k_y^2k_x)\sigma_z \quad (39)$$

Applying this Hamiltonian to the Dirac spinor $\begin{pmatrix} \psi_1 \\ \psi_2 \end{pmatrix}$ and making the substitution $k_x \rightarrow -i\partial_x$ yields the following Schrodinger system of equations for the region $x < 0$, where there is no added potential:

$$-v(\partial_x + k_y)\psi_2 + i\lambda(\partial_x^3 + 3k_y^2\partial_x)\psi_1 = E\psi_1 \quad (40)$$

$$v(\partial_x - k_y)\psi_1 - i\lambda(\partial_x^3 + 3k_y^2\partial_x)\psi_2 = E\psi_2 \quad (41)$$

We now apply this to our ansatz wavefunctions, as before. In this case, we will use the same ansatz as in [5] and section 4.1, but we first show that this ansatz is appropriate to this new problem. We apply the Hamiltonian to the more general ansatz, $\psi_1 = e^{ik_x x} + r e^{-ik_x x}$ and $\psi_2 = A e^{ik_x x} + B e^{-ik_x x}$. Applying (40) to the ansatz and collecting terms in $e^{ik_x x}$ and $e^{-ik_x x}$ yields:

$$e^{ik_x x} [E + Av(ik_x + k_y) - \lambda(k_x^3 - 3k_y^2 k_x)] + e^{-ik_x x} [Er + vB(ik_x + k_y) + r\lambda(k_x^3 - 3k_y^2 k_x)] = 0$$

$$-Aivk_F e^{-i\phi} + \lambda k_F^3 \cos(3\phi) = E \quad \text{and} \quad \frac{B}{r} ivk_F e^{i\phi} - \lambda k_F^3 \cos(3\phi) = E \quad (42)$$

Adding these two equations and substituting $v = |E|/k_F$ yields:

$$Ae^{-i\phi} - \frac{B}{r} e^{i\phi} = -\frac{2E}{i|E|} = 2i \operatorname{sgn}(E) = 2s$$

Rearranging, we have

$$\frac{A}{s} e^{-i\phi} - \frac{B}{rs} e^{i\phi} = 2$$

and since $e^{-i\phi}$ and $e^{i\phi}$ are linearly independent and this equation holds for all ϕ , we obtain the relations

$$A = s e^{i\phi} \quad \text{and} \quad B = -r s e^{-i\phi} \quad \text{where } s = i \operatorname{sgn}(E) \quad (43)$$

Putting these expressions for A and B back into equations (42) yields the Schrodinger equations:

$$-ivsk_F + \lambda k_F^3 \cos(3\phi) = E \quad \text{and} \quad -ivsk_F - \lambda k_F^3 \cos(3\phi) = E \quad (44)$$

For either of these equations, we can multiply both sides by its complex conjugate to obtain:

$$E = \pm \sqrt{(vk_F)^2 + \lambda^2 k_F^6 \cos^2(3\phi)} \quad (45)$$

This is the result in [7]. In Figure 9, we show a constant energy contour plot of this result, much like that in [7] and see that at low energies, the Fermi surface looks like that of a simple Dirac Hamiltonian that we have been considering throughout the paper, but that at higher energies, we see the hexagonal warping of the Fermi surface.

5.1.2 Inside the Barrier, $0 < x < D$

We next turn our attention to the Hamiltonian inside the barrier, apply the most general ansatz, and solve for the coefficients and q_x as we've done in the simple Dirac case. Inside the barrier, our Schrodinger

equations are:

$$-v(\partial_x + k_y)\psi_2 + i\lambda(\partial_x^3 + 3k_y^2\partial_x)\psi_1 = (E - V_0)\psi_1 \quad (46)$$

$$v(\partial_x - k_y)\psi_1 - i\lambda(\partial_x^3 + 3k_y^2\partial_x)\psi_2 = (E - V_0)\psi_2 \quad (47)$$

Now let's apply our ansatz, $\psi_1 = ae^{iq_x x} + be^{-iq_x x}$ and $\psi_2 = ce^{iq_x x} + de^{-iq_x x}$. Plugging this into Equation (46), yields:

$$e^{ik_x x}[a(E - V_0 - \lambda(q_x^3 - 3k_y^2 q_x)) + vc(iq_x + k_y)] + e^{-ik_x x}[b(E - V_0 + \lambda(q_x^3 - 3k_y^2 q_x)) + vd(iq_x + k_y)] = 0$$

$$-v\frac{c}{a}(iq_x + k_y) = E - V_0 - \lambda(q_x^3 - 3k_y^2 q_x) \quad (48)$$

$$-v\frac{d}{b}(-iq_x + k_y) = E - V_0 + \lambda(q_x^3 - 3k_y^2 q_x) \quad (49)$$

Furthermore, plugging in the ansatz to Equation (47) yields similar equations:

$$v\frac{a}{c}(iq_x - k_y) = E - V_0 + \lambda(q_x^3 - 3k_y^2 q_x) \quad (50)$$

$$v\frac{b}{d}(-iq_x - k_y) = E - V_0 - \lambda(q_x^3 - 3k_y^2 q_x) \quad (51)$$

From (48) and (50) we have

$$c = \frac{av(iq_x - k_y)}{E - V_0 + \lambda(q_x^3 - 3k_y^2 q_x)} = \frac{-vc(iq_x + k_y)}{E - V_0 - \lambda(q_x^3 - 3k_y^2 q_x)} \cdot \frac{v(iq_x - k_y)}{E - V_0 + \lambda(q_x^3 - 3k_y^2 q_x)}$$

so that

$$q_x^2 + k_y^2 = \frac{1}{v^2}[(E - V_0)^2 - \lambda^2(q_x^3 - 3k_y^2 q_x)^2] \quad (52)$$

gives an expression for q_x . Next, we add (48) and (49), as before in the out-of-barrier case, making the substitutions of $q_x = k'_F \cos \theta$, $k_y = k'_F \sin \theta$, and $v = |E - V_0|/k'_F$ to obtain:

$$\frac{c}{a}e^{-i\theta} - \frac{d}{b}e^{i\theta} = -\frac{2(E - V_0)}{ivk'_F} = \frac{2i(E - V_0)}{|E - V_0|} = 2s'$$

where we've defined $s' = i\text{sgn}(E - V_0)$. Rearranging and noting that $e^{i\theta}$ and $e^{-i\theta}$ are linearly independent, we obtain expressions for c and d :

$$c = ase^{i\theta} \quad \text{and} \quad d = -bse^{-i\theta} \quad (53)$$

where of course by definition, $\theta = \arctan(k_y/q_x)$.

5.1.3 Outside the Barrier, $x > D$

Lastly, we consider the region to the right of the barrier, governed by the system of Schrodinger equations of Equations (40) and (41), and we plug in the general ansatz in this region, $\psi_1 = te^{ik_x x}$, $\psi_2 = ue^{ik_x x}$,

since in this region there is no backward traveling wave. Using the same procedure as above, we obtain the equations

$$\begin{aligned} -v\frac{u}{t}(ik_x + k_y) + \lambda^2(k_x^3 - 3k_y^2k_x)^2 &= E \\ v\frac{t}{u}(ik_x - k_y) - \lambda^2(k_x^3 - 3k_y^2k_x)^2 &= E \end{aligned}$$

Adding the two equations, as before, yields:

$$-\frac{u}{t}e^{-i\phi} + \frac{t}{u}e^{i\phi} = \frac{2E}{ik_Fv} = -2i\text{sgn}(E) = -2s$$

where we define s as before. We thus obtain an expression for u :

$$u = ste^{i\phi}$$

5.2 Barrier of Height V_0 , Rotated by $\pi/6$ (Along ΓM)

Again, we wish to apply the same formalism as before, but now we rotate the Hamiltonian by an angle of $\pi/6$ in k -space to examine the effect of the hexagonal warping on the barrier transmission, when the barrier is placed at an angle to the coordinate axes. Since we wish to place the barrier displaced by $\pi/6$, we rotate the k_x and k_y directions by $-\pi/6$. Our original Schrodinger equations are given by:

$$\begin{aligned} -v(ik_x + k_y)\psi_2 + \lambda(k_x^3 - 3k_y^2k_x)\psi_1 &= E\psi_1 \\ v(ik_x - k_y)\psi_1 - \lambda(k_x^3 - 3k_y^2k_x)\psi_2 &= E\psi_2 \end{aligned}$$

We now substitute in k'_x and k'_y for k_x and k_y , where k'_x and k'_y are the rotated coordinates, given by:

$$\begin{pmatrix} k'_x \\ k'_y \end{pmatrix} = \begin{pmatrix} \cos(-\frac{\pi}{6}) & -\sin(-\frac{\pi}{6}) \\ \sin(-\frac{\pi}{6}) & \cos(-\frac{\pi}{6}) \end{pmatrix} \begin{pmatrix} k_x \\ k_y \end{pmatrix} = \begin{pmatrix} \frac{\sqrt{3}}{2}k_x + \frac{1}{2}k_y \\ \frac{\sqrt{3}}{2}k_y - \frac{1}{2}k_x \end{pmatrix}$$

Our new Schrodinger equations become:

$$\begin{aligned} -vw(ik_x + k_y)\psi_2 - \lambda(k_y^3 - 3k_x^2k_y)\psi_1 &= E\psi_1 \\ vw^\dagger(ik_x - k_y)\psi_1 - \lambda(k_y^3 - 3k_x^2k_y)\psi_2 &= E\psi_2 \end{aligned}$$

with $w = \frac{\sqrt{3}}{2} + \frac{1}{2}i$. So we now proceed exactly as in Section 5.1, applying this to our generic ansatz wavefunctions. We replace k_x by $-\partial_x$ and obtain:

$$-vw(\partial_x + k_y)\psi_2 - \lambda(k_y^3 + 3\partial_x^2k_y)\psi_1 = E\psi_1 \quad (54)$$

$$vw^\dagger(\partial_x - k_y)\psi_1 + \lambda(k_y^3 + 3\partial_x^2k_y)\psi_2 = E\psi_2 \quad (55)$$

$$(56)$$

5.2.1 Outside the Barrier, $x < 0$

We now apply our rotated Schrodinger equations to the general ansatz, $\psi_1 = e^{ik_x x} + r e^{-ik_x x}$ and $\psi_2 = A e^{ik_x x} + B e^{-ik_x x}$. We obtain two equations (one for $e^{ik_x x}$, one for $e^{-ik_x x}$) for each of the two equations above, yielding four equations:

$$-A w v i k_F e^{-i\phi} - \lambda(k_y^3 - 3k_x^2 k_y) = E \quad (57)$$

$$-\frac{b}{r} w v i k_F e^{i\phi} - \lambda(k_y^3 - 3k_x^2 k_y) = E \quad (58)$$

$$\frac{1}{A} v w^\dagger i k_F e^{i\phi} + \lambda(k_y^3 - 3k_x^2 k_y) = E \quad (59)$$

$$-\frac{r}{B} v w^\dagger i k_F e^{-i\phi} + \lambda(k_y^3 - 3k_x^2 k_y) = E \quad (60)$$

Adding Equations (57) and (59) yields:

$$-A w e^{-i\phi} + \frac{w^\dagger}{A} e^{i\phi} = \frac{2E}{v i k_F} = -2i \text{sgn}(E) = -2s$$

whence we obtain an expression for A: $A = \frac{s}{w} e^{i\phi}$. Similarly, we add Equations (58) and (60) to obtain:

$$\frac{B}{r} w e^{i\phi} - \frac{r}{B} w^\dagger e^{-i\phi} = \frac{2E}{v i k_F} = -2i \text{sgn}(E) = -2s$$

whence we obtain $B = -r \frac{s}{w} e^{-i\phi}$.

5.2.2 Inside the Barrier

In this region, our Schrodinger equations are much the same, except we replace E with $E - V_0$ to account for the barrier height:

$$\begin{aligned} -v w (\partial_x + k_y) \psi_2 - \lambda(k_y^3 + 3\partial_x^2 k_y) \psi_1 &= (E - V_0) \psi_1 \\ v w^\dagger (\partial_x - k_y) \psi_1 + \lambda(k_y^3 + 3\partial_x^2 k_y) \psi_2 &= (E - V_0) \psi_2 \end{aligned}$$

We now apply these to the general ansatz $\psi_1 = a e^{iq_x x} + b e^{-iq_x x}$ and $\psi_2 = c e^{iq_x x} + d e^{-iq_x x}$ to obtain again four equations:

$$-\frac{c}{a} v w (iq_x + k_y) - \lambda(k_y^3 - 3q_x^2 k_y) = E - V_0 \quad (61)$$

$$-\frac{d}{b} v w (-iq_x + k_y) - \lambda(k_y^3 - 3k_x^2 k_y) = E - V_0 \quad (62)$$

$$\frac{a}{c} v w^\dagger (iq_x - k_y) + \lambda(k_y^3 - 3k_x^2 k_y) = E - V_0 \quad (63)$$

$$-\frac{b}{d} v w^\dagger (iq_x + k_y) + \lambda(k_y^3 - 3k_x^2 k_y) = E - V_0 \quad (64)$$

Making the substitutions $iq_x + ky = ik'_F e^{-i\theta}$ and $iq_x - ky = ik'_F e^{i\theta}$, and adding Equations (61) and (63) yields:

$$\frac{a}{c} w^\dagger e^{i\theta} - \frac{c}{a} w e^{-i\theta} = \frac{2E}{vik'_F} = -2i \text{sgn}(E - V_0) = -2s'$$

whence we obtain $c = a \frac{s'}{w} e^{i\theta}$. Similarly, adding Equations (62) and (64) yields:

$$\frac{d}{b} w e^{i\theta} - \frac{b}{d} w^\dagger e^{-i\theta} = \frac{2E}{vik'_F} = -2i \text{sgn}(E - V_0) = -2s'$$

whence we obtain $d = -b \frac{s'}{w} e^{-i\theta}$. We now seek an equation for q_x , which we obtain by solving (61) for c and plugging into (63). From (61),

$$c = -a \frac{E - V_0 + \lambda(k_y^3 - 3q_x^2 k_y)}{vw(iq_x + k_y)}$$

and substituting this into (63) yields an expression which we can solve for q_x :

$$q_x^2 + k_y^2 = \frac{1}{v^2} ((E - V_0)^2 - \lambda^2 (k_y^3 - 3q_x^2 k_y)^2)$$

5.2.3 Outside the Barrier, $x > D$

Finally, we consider the region following the barrier and apply our Schrodinger equations, (54) and (55), to the general ansatz wavefunctions $\psi_1 = t e^{ik_x x}$ and $\psi_2 = u e^{ik_x x}$. We obtain now two equations (since we no longer have the reflection terms $e^{-ik_x x}$):

$$\begin{aligned} -\frac{u}{t} v w i k_F e^{-i\phi} - \lambda(k_y^3 - 3q_x^2 k_y) &= E - V_0 \\ \frac{t}{u} v w^\dagger i k_F e^{i\phi} + \lambda(k_y^3 - 3q_x^2 k_y) &= E - V_0 \end{aligned}$$

Adding these two equations gives

$$v i k_F \left(\frac{t}{u} w^\dagger e^{i\phi} - \frac{u}{t} w e^{-i\phi} \right) = 2(E - V_0)$$

whence we obtain $u = t \frac{s'}{w} e^{i\phi}$.

5.3 Comparison of Transmission Coefficients: Simple Dirac, k^3 with Barrier along ΓM , k^3 with Barrier along ΓK

We now proceed as before, calculating r , the reflection amplitude and using it to find R and thus T , the reflection and transmission coefficients as a function of barrier height and incident angle for a given energy. This is identical to the case of the simple Dirac Hamiltonian, except we use different expressions for s and q_x , as specified by the results in the preceding sections. We show plots of the transmission coefficient, T , as a function of incident angle ϕ for several different energies in each of the three cases discussed: simple Dirac, k^3 with the barrier along the ΓM direction (above, the rotated case), and k^3 with the barrier along the ΓK direction. In Figure 9, we display the constant energy contours

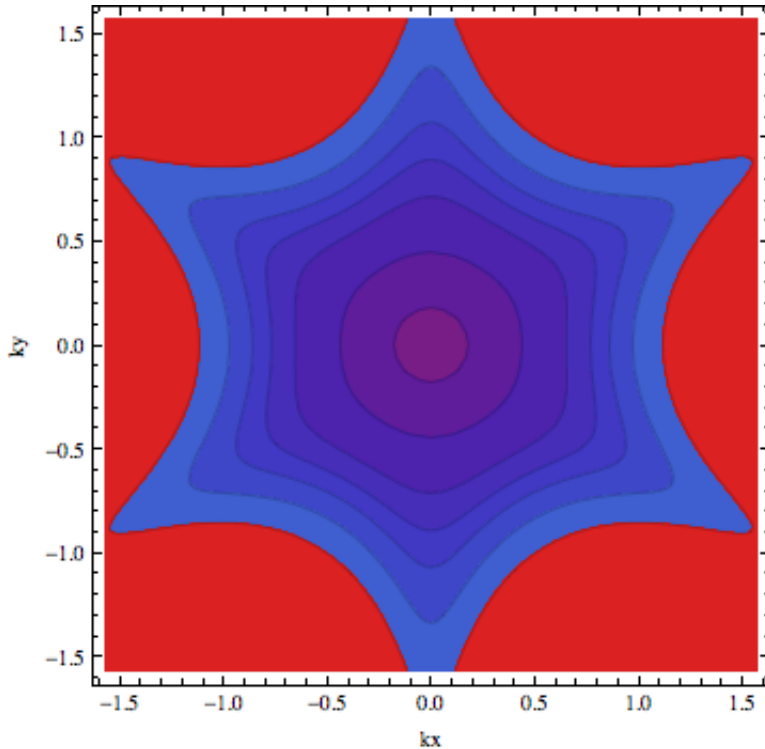


Figure 9: Energy contour plot of the k^3 Hamiltonian in the units of $\sqrt{v/\lambda}$

of the k^3 Hamiltonian at which we plot the transmission in Figures 10,11, and 12. These energies, $0.2E^*, 0.5E^*, 0.8E^*, E^*, 1.2E^*, 1.5E^*$, and $2E^*$, with $E^* = 0.23\text{eV}$, as can be seen in the Figure, span the energy range from a conic dispersion to the hexagonally warped region. At lower energies, the simple Dirac Hamiltonian, and warped Hamiltonians with barriers along ΓK and ΓM all produce similar transmission results. As we increase the energies, however, the transmission along the ΓK direction changes due to the distorted Fermi surface.

In this independent work paper, we began with a two-dimensional topological insulator, HgTe, and studied the effects of inversion and time-reversal breaking terms when applied to the edge. We found that in the presence of a magnetic impurity, the edge modes do not reconstruct, but are destroyed at the edge where the impurity is applied, opening a gap in the spectrum. We additionally extended these results to the quasi-two-dimensional topological insulator case and visualized Dirac cones in our simulation. We then turned our attention to the surfaces of 3D topological insulators and developed a framework for computing transmission coefficients for a step-barrier potential. We also showed the results of these computations for varying incident angles and barrier heights. Lastly, in this section we have introduced, following [7], a hexagonal distortion term to the Dirac Hamiltonian and applied the potential barrier analysis from the previous sections to this new Hamiltonian. We found that at higher energies, where hexagonal warping is apparent, barriers along the ΓM and ΓK produce different transmission coefficient profiles as a function of incident angle, suggesting that scattering is different along these two different directions.

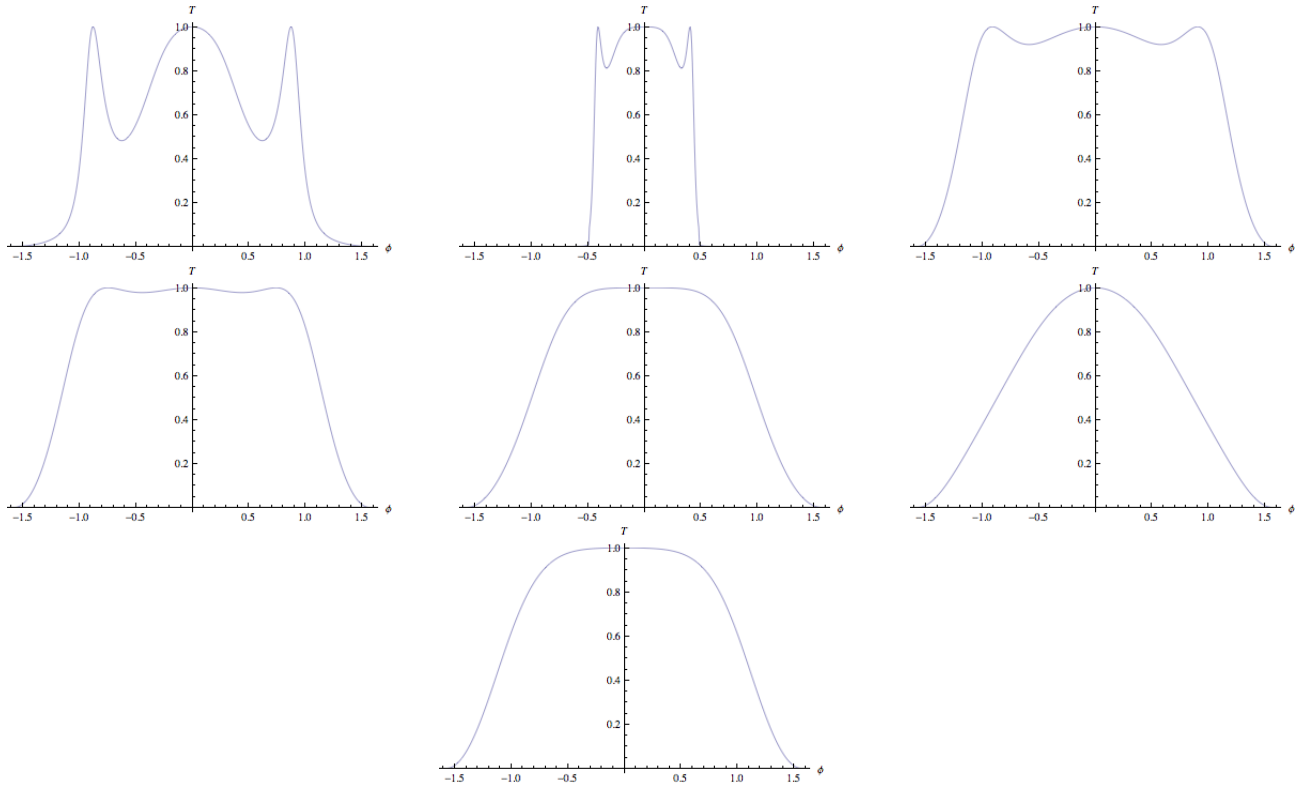


Figure 10: Plots of transmission coefficients T as a function of incident angle ϕ in the simple Dirac case for barrier heights of $V_0 = 0.1$ eV, and energies $0.2E^*, 0.5E^*, 0.8E^*, E^*, 1.2E^*, 1.5E^*$, and $2E^*$, with $E^* = 0.23$ eV.

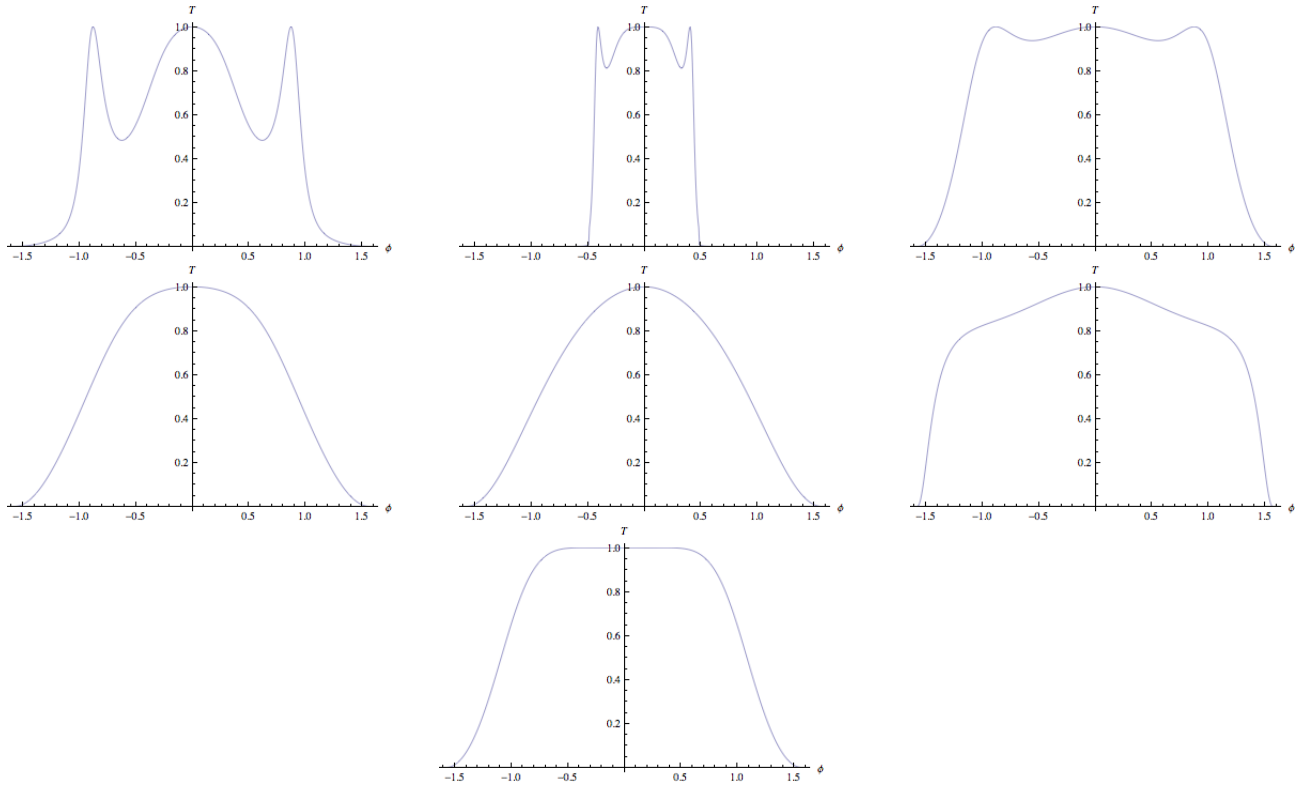


Figure 11: Plots of transmission coefficients T as a function of incident angle ϕ in the simple k^3 case with barrier along ΓM , for barrier heights of $V_0 = 0.1$ eV, and energies $0.2E^*, 0.5E^*, 0.8E^*, E^*, 1.2E^*, 1.5E^*$, and $2E^*$, with $E^* = 0.23$ eV.

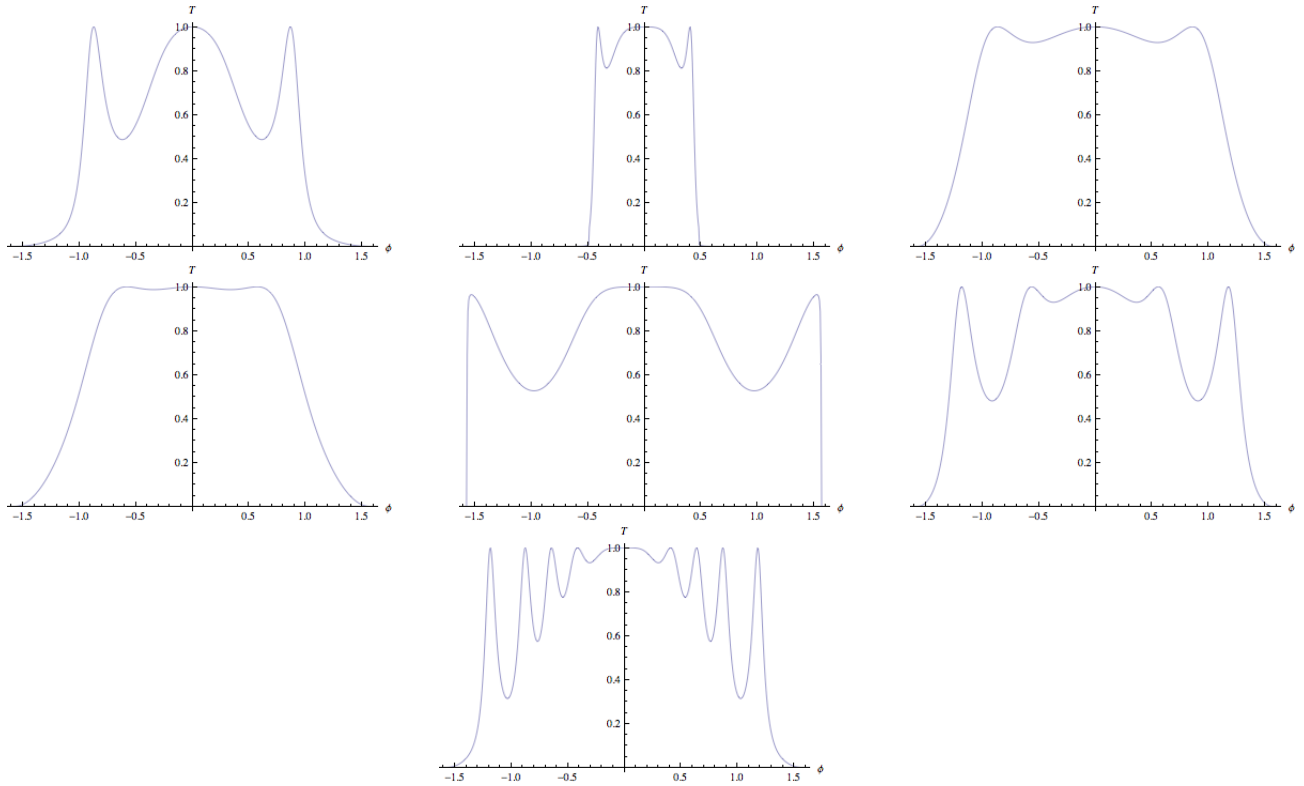


Figure 12: Plots of transmission coefficients T as a function of incident angle ϕ in the simple k^3 case with barrier along ΓK , for barrier heights of $V_0 = 0.1$ eV, and energies $0.2E^*$, $0.5E^*$, $0.8E^*$, E^* , $1.2E^*$, $1.5E^*$, and $2E^*$, with $E^* = 0.23$ eV.

References

- [1] Bernevig, B. A., T. H. and Zhang, S.-C. *Science* **314**, 1757–1761 (2006).
- [2] Hsieh, D. e. a. *Nature* **452**, 970 (2008).
- [3] Kane, C. and Mele, E. *Physical Review Letters* **95**, 246802 (2005).
- [4] Pedram Roushan, Jungpil Seo, C. V. P. Y. H. D. H. D. Q. A. R. M. H. R. C. and Yazdani, A. *Nature* **460**, 1106,1109 (2009).
- [5] Katsnelson, M., Novoselov, K., and Geim, A. *Nature Physics* **2** September (2006).
- [6] *New Advances in Condensed Matter Physics: Lecture 18*, B. Andrei Bernevig, PHY536 Lecture Notes, Princeton University, Spring 2010.
- [7] *Hexagonal Warping Effects in the Surface States of Topological Insulator Bi₂Te₃*, Liang Fu, arXiv:0908.1418v3.